Environmental Research 231 (2023) 116146

Contents lists available at ScienceDirect

Environmental Research

journal homepage: www.elsevier.com/locate/envres

Pyrolyzed magnetic NiO/carbon-derived nanocomposite from a hierarchical nickel-based metal-organic framework with ultrahigh adsorption capacity

Negar Beigi [a], Hadi Shayesteh [b], Shahrzad Javanshir [c], Majid Hosseinzadeh [a,*]

[a] School of Civil Engineering, Iran University of Science and Technology, Narmak, Tehran, Iran
[b] School of Chemical, Petroleum and Gas Engineering, Iran University of Science and Technology, Narmak, Tehran, Iran
[c] Pharmaceutical and Heterocyclic Compounds Research Laboratory, Chemistry Department, Iran University of Science and Technology, Narmak, Tehran, Iran

ARTICLE INFO

Keywords:
Metal-organic framework
Porous carbon nanocomposite
Pyrolysis
Adsorption
Dye

ABSTRACT

Herein, a simple one-pot solvothermal approach is used to create magnetic porous carbon nanocomposites which obtained from a nickel-based metal-organic framework (Ni-MOF) and examined for their ability to uptake methyl orange (MO) dye. Derived carbons with exceptional porosity and magnetic properties were created during the different pyrolysis temperatures of Ni-MOF (700, 800, and 900 °C) under a nitrogen atmosphere. The black powders were given the names CDM-700, CDM-800, and CDM-900 after they were obtained. A variety of analysis methods, including FESEM, EDS, XRD, FTIR, VSM, and N_2 adsorption-desorption were used to characterize as-prepared powders. Furthermore, adsorbent dosage, contact time, pH variation, and initial dye concentration effects was investigated. The maximum adsorption capacities were 307.38, 5976.35, 4992.39, and 2636.54 mg/g for Ni-MOF, CDM-700, CDM-800, and CDM-900, respectively, which show the ultrahigh capacity of the resulted nanocomposites compared to newest materials. The results showed that not only the crystallinity turned but also the specific surface area was increased about four times after pyrolyzing. The results showed that the maximum adsorption capacity of MO dye for CDM-700 was obtained at adsorbent dosage of 0.083 g/L, contact time of 60 min, feed pH of 3, and temperature of 45 °C. The Langmuir model has the best match and suggests the adsorption process as a single layer. According to the results of reaction kinetic studies using well-known models, the pseudo-second-order model (R^2 = 0.9989) displayed high agreement with the experimental data. The synthesized nanocomposite is introduced as a promising superadsorbent for eliminating dyes from contaminated water due to strong recycling performance up to the fifth cycle.

1. Introduction

Nowadays, one of the biggest environmental problems directly related to human life and health is drinking water pollution due to the extensive development of industrial and economic activities. Discharging chemical dyes from various industrial units such as plastic processing industries, paper production, textiles and coatings, and paints into wastewaters has created widespread communities concern about water pollution (Chin et al., 2018; Nazir et al., 2021b). Methyl orange dye is used as an example of these organic dyes, which has endless use in laboratory experiments, industrial products, and textiles, and contact with it has incredible effects such as the shock, quadriplegia, cyanosis, tissue necrosis, vomiting, jaundice, and increase in heart rate on the human body (Nazir et al., 2021b). As a result, removing organic dyes from contaminated water before releasing them into the environment is a crucial process.

Considering the comprehensive effects of water pollution, various methods and techniques such as membrane separation (Tran et al., 2019), photodegradation (Yang et al., 2015), adsorption (Ahmad et al., 2021; Nazir et al., 2021a), coagulation (Ren et al., 2019), ozonolysis, chlorination (Ahmad et al., 2020), electrochemical process (Pacheco-Álvarez et al., 2019), chemical oxidation (Arslan et al., 2000), photo-oxidation (Kim et al., 2017), advanced oxidation processed (AOPs) (Xi et al., 2014), and microbial anaerobic degradation (Lu et al., 2019; Solís et al., 2012) have been introduced to eliminate pollutants. The adsorption technique is presented as one of the most appropriate

* Corresponding author.
E-mail addresses: Beigi_negar@civileng.iust.ac.ir, beigi.negar98@gmail.com (N. Beigi), Hadi.shayesteh91@gmail.com, Hadi_shayesteh@chemeng.iust.ac.ir (H. Shayesteh), Shjavan@iust.ac.ir (S. Javanshir), Hosseinzadeh_m@iust.ac.ir (M. Hosseinzadeh).

https://doi.org/10.1016/j.envres.2023.116146
Received 27 January 2023; Received in revised form 15 April 2023; Accepted 13 May 2023
Available online 13 May 2023
0013-9351/

and reliable techniques for removing all kinds of toxic dyes, because of its simplicity, high efficiency, and low-cost (del Rio et al., 2022; Nazir et al., 2021b). Among efficient adsorbents, porous materials have been proposed as one of the most efficient strategies to removal water contaminants (Alsbaiee et al., 2016; Samanta et al., 2019). Various porous materials such as hydrotalcite (Lazaridis et al., 2003), zeolites (Jiang et al., 2018), silica-based mesoporous materials (Costa et al., 2020), and activated carbons (Cabrita et al., 2010) have been considered for treating wastewater. These materials adsorb organic contaminants by a number of distinct methods, or a combination of them, including hydrogen bonding, π - π stacking, hydrophobic interactions, electrostatic interactions, and acid-base interactions (Dai et al., 2019; Hasan and Jhung, 2015; Huang et al., 2020).

Metal-organic frameworks (MOFs) have attracted the wide attention of researchers in the field of adsorption of various pollutants, including organic dyes, heavy metals, pharmaceutical, and harmful materials, due to their enormous surface area, high porosity with variable pore size, flexibility, adaptability, and tailored chemical functionalities (Chen et al., 2019; Dhaka et al., 2019; Nazir et al., 2021b). Metal ions or clusters serve as nodes in MOF structures, with organic ligands serving as linkers for the coordination bonds between the nodes (Asgharinezhad and Ebrahimzadeh, 2021; Majano and Pérez-Ramírez, 2013). Among nanoporous materials, MOFs are a continuously growing category because of the diversity of metals and organic binders that are available, along with the potential for their chemical functionalization and combination (del Rio et al., 2022). Additionally, owing to their outstanding properties and future potential applications, MOFs have gained great popularity in various fields such as catalysis (Tsiakaras, 2022), air filtration (Zhang et al., 2019), chemical sensing, drug delivery (Shah et al., 2017), adsorption (Khan et al., 2021; Nazir et al., 2021b), energy storage (Hussain et al., 2020), oxygen reduction reaction (Najam et al., 2019), noise reduction (Zhang et al., 2020), molecule separation, and gas storage (Ahmad et al., 2020). Two major barriers to the utilization of MOFs in pollutant removal are their fragility in some aquatic habitats and their time-consuming separation after batch adsorption, which needs lengthy centrifugation and separting methods (Nazir et al., 2021b). The MOF precursor serves as an effective carbon supply during the pyrolysis of MOFs in an inert atmosphere, resulting in porous carbon structures that are impregnated with linker-derived heteroatoms and the metal ions or clusters are distributed as metallic nanoparticles or metal oxide throughout the carbonaceous framework (Yan et al., 2014). Carbons generated from MOFs have active sites with large specific surfaces and high porosities that quickly enrich the target pollutants, which is a beneficial factor for complete and fast further degradation of pollutants, with the advantage that is more chemically stable than precursor MOFs (del Rio et al., 2022). Along with these qualities, the rise in interactions with the aromatic rings of organic molecules promotes the promising utilization of porous carbons for the adsorption of organic pollutants (Asgharinezhad and Ebrahimzadeh, 2021; del Rio et al., 2022). Metal ions can be changed into metal oxides by calcining MOFs at mild temperatures, and the emission of gas during the calcination process results in oxides with linked pores (Asgharinezhad and Ebrahimzadeh, 2021). As a result, the creation of metal oxides from MOFs is a superior method due to their distinctive structure and large surface area. Moreover, since pyrolysis of MOFs results in the development of metal or metal-carbon composites, using MOFs with various metal centers as precursors enables the production of porous carbon with a variety of characteristics (del Rio et al., 2022). For instance, Tahazadeh et al. used carbon derived from MOF-5 as an adsorbent nanoparticle in the preparation of nanocomposite membranes to adsorb methylene blue dye. According to the report's results, under optimal test conditions, there was an excellent adsorption efficiency (87.72%) and a reasonable adsorption capacity (41.36 mg/g) (Tahazadeh et al., 2021). Gan et al. used MOF-74(Zn) loaded with Fe_2O_3 to adsorb Bisphenol A. Magnetic carbon nanotubes derived from MOF-74(Zn) with non-magnetic state was compared and it was found that the maximum adsorption with this adsorbent was higher than the reports mentioned for other adsorbents (Gan et al., 2021). Besides, Yanga et al. synthesized flower-like hierarchical Ni–Zn MOF microspheres through a thermal solvent method to adsorb congo red dye. Based on the data, the adsorption capacity of mixed metals Ni and Zn was about 2 and 3 times of Ni-MOF and Zn-MOF, respectively (Yang and Bai, 2019).

In order to effectively spread the sorbent in a wider sample volume and recover it using an external magnet after usage for contamination removal, magnetically porous carbon can be produced by employing precursors such as iron or nickel metal-organic frameworks (Asgharinezhad and Ebrahimzadeh, 2021). Herein, for the first time the ability of synthesized nickel-based MOF and its carbon derived have been compared on the adsorption capacity for removing methyl orange dye from the aqueous solution. Furthermore, adsorbent dosage, contact time, pH variation, and initial dye concentration effects was investigated in detail. Additionally, kinetic and isotherm studies were evaluated using various common models.

2. Materials and methods

2.1. Reagents

N, N-dimethylformamide (DMF), Nickel nitrate hexahydrate ($Ni(NO_3)_2{\cdot}6H_2O$), and ethanol were purchased from Merck Co. With analytical grade. Terephthalic acid and methyl orange were also supplied by Merck.

2.2. Synthesis of Ni-based MOF

Ni-MOF was prepared using a solvothermal method. Typically, $Ni(NO_3)_2$ (2 mmol), and terephthalic acid (2 mmol) were dispersed in the distilled water (2.5 mL), DMF (35 mL), and ethanol (2.5 mL) mixture. The solution was poured into a 120 mL Teflon-lined autoclave after mixing for 60 min and a light green precipitate would be formed after maintaining at 120 °C for 420 min. Finally, the solid was screened and repeatedly methanol washed, and then dried at 60 °C overnight. All solutions for every session of experimentation were freshly prepared.

2.2.1. Synthesis of MOF-derived carbons

The synthetic Ni-MOF was directly heated for 2.5 h at temperatures of 700, 800, and 900 °C (at a rate of 5 °C/min) in a tube furnace using nitrogen gas to produce the porous carbons (CDMs). The as-obtained black powders at 700, 800, and 900 °C were named CDM-700, CDM-800, and CDM-900, respectively, and the yield of CDM-700, CDM-800, and CDM-900 was 0.72, 0.54, and 0.31 g for 1 g of Ni-MOF, respectively.

2.3. Adsorption procedure

MO dye was employed as a wastewater-contaminated sampel to assess adsorption effectiveness of the Ni-MOF and its derived carbons. Typically, as-prepared MOFs (Ni-MOF, CDM-700, CDM-800, and CDM-900) were added into 30 mL of MO aqueous solution (50 mg/L). The obtained suspension was sonicated using an ultrasonic bath (35 kHz) for regular intervals. After reaching the equilibrium time, particles were separated with a centrifuge device for Ni-MOF (10 min at 12,000 rpm) and using a magnet for derived carbons. The residual concentration of MO was measured using a UV–visible spectrophotometer (Shimadzu, Japan) at $\lambda_{max} = 464$ nm. MO amount adsorbed at any time q (mg/g) could be defined as the following (Eq. (1)):

$$q = \frac{(C_0 - C_t)V}{W} \quad (1)$$

The removal efficiency can be calculated by following Eq. (2):

$$R(\%) = \frac{C_0 - C_f}{C_0} \times 100 \quad (2)$$

3. Results and discussion

3.1. Characterization

The crystal structures of the Ni-MOF and CDMs are shown in Fig. 1 by the XRD patterns of the as-prepared samples. Three primary diffraction peaks at 2θ = 8.6, 14.9, and 15.9° correspond to the (100), (010), and (020) planes, respectively are depicted in Fig. 1(a) (Lu and Wu, 2018; Zhang et al., 2015). Fig. 1(b) shows the CDMs' XRD patterns at various pyrolysis temperatures. When compared to the face-centered cubic phase (FCC) of the Ni metal (JCPDS No. 04–0850), it showed three Sharp peaks at 44.5°, 51.7°, and 76.3°, which can be represented by the (111), (200), and (220) crystal faces of the Ni metal, respectively (Shayesteh et al., 2022). Furthermore, the fact that the CDMs structure is still crystallized after pyrolysis and that no other phase exists except for the face-centered cubic Ni metal and carbon even at each pyrolysis temperature suggests that Ni ions can be entirely converted to Ni metal during the carbonization process of Ni-MOF. It can be deduced that some Ni nanocrystals preferentially orient under the external magnetic field along the (111) axis direction because of having a high intensity compared to other peaks (200, 220) (Hemmati et al., 2016).

The group functional of as-prepared materials is determined by using FTIR analysis (Fig. 2). The sharp bands of Ni-MOF located at 746–822, 1358, and 1582 cm^{-1} illustrating Ni–O, carboxyl vibration mode, C═C band, respectively (Neisi et al., 2019; Srivind et al., 2019; Sudhasree et al., 2014). The peaks related to O–H can be observed at 3522 and 3592 cm^{-1} [44]. The C–H stretching vibrational modes of the CH_2 and CH_3 can be attributed to the weak bands at 2372 and 2926, respectively (Eluri and Paul, 2012; Wang et al., 2008). Additionally C–O stretching was prominently featured in 800–1200 cm^{-1} (Fig. 2(a)) (Shayesteh et al., 2022). After pyrolysis of Ni-MOF at different temperatures, various important bands were obtained at 3430, 2920, 2850, 1722, 1624, 1374, 1166, 586, and 470 cm^{-1} (Fig. 2(b)). The broad peak of hydroxyl groups (O–H) appeared at 3430 cm^{-1} [44]. Besides, the Ni–O group vibration can be attributed to the bands at 450–600 cm^{-1} (Srivind et al., 2019). Similar to Ni-MOF, two functional groups include the C–H stretching bands of CH_2 and CH_3 can be found at 2920 and 2850 cm^{-1} (Eluri and Paul, 2012; Wang et al., 2008). Furthermore, in the range of 1200–1750 cm^{-1}, the group functionals C═O, O–C═O, and C═C appeared (Sudhasree et al., 2014).

The morphology of Ni-MOF and its carbon derived as well as EDX analyses were shown in Fig. 3. The structure of Ni-MOF was created from various petal-shaped nanosheets that compacted to each other with

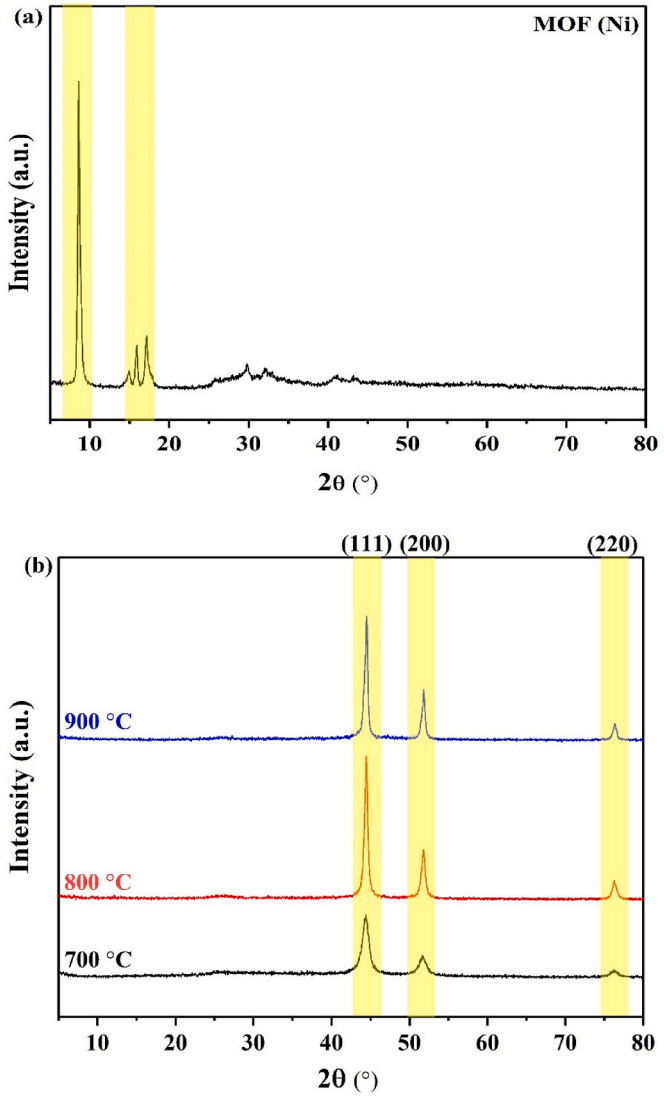

Fig. 1. XRD patterns of (a) Ni-MOF and (b) MOF-derived porous carbon nanocomposites.

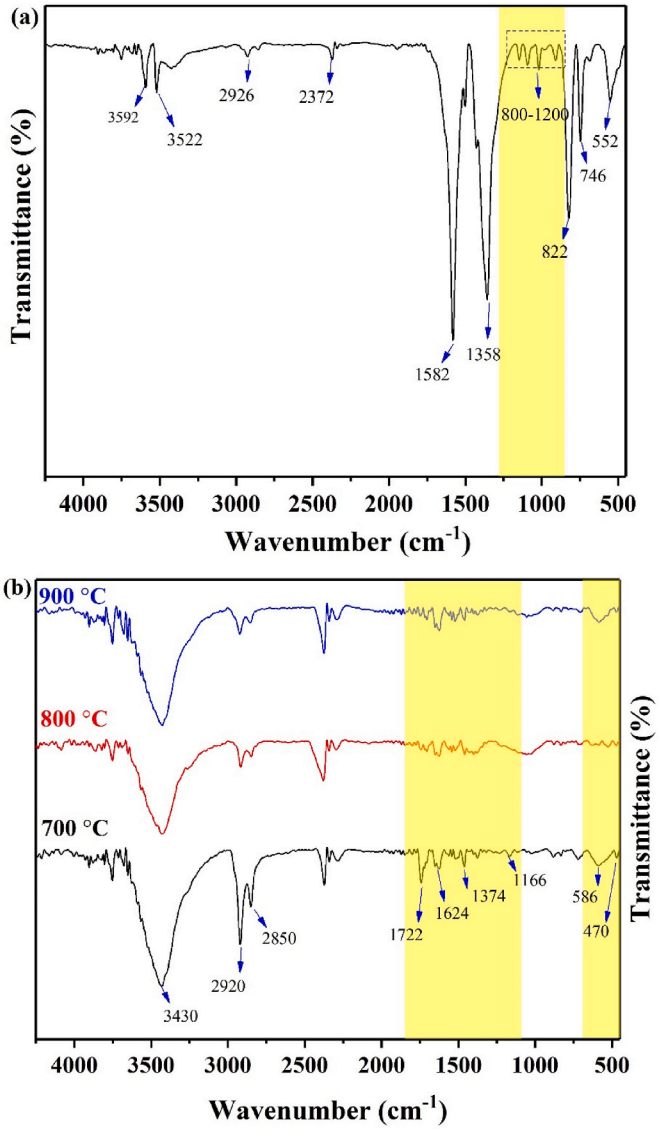

Fig. 2. FTIR spectrum of (a) Ni-MOF and (b) MOF-derived porous carbon nanocomposites.

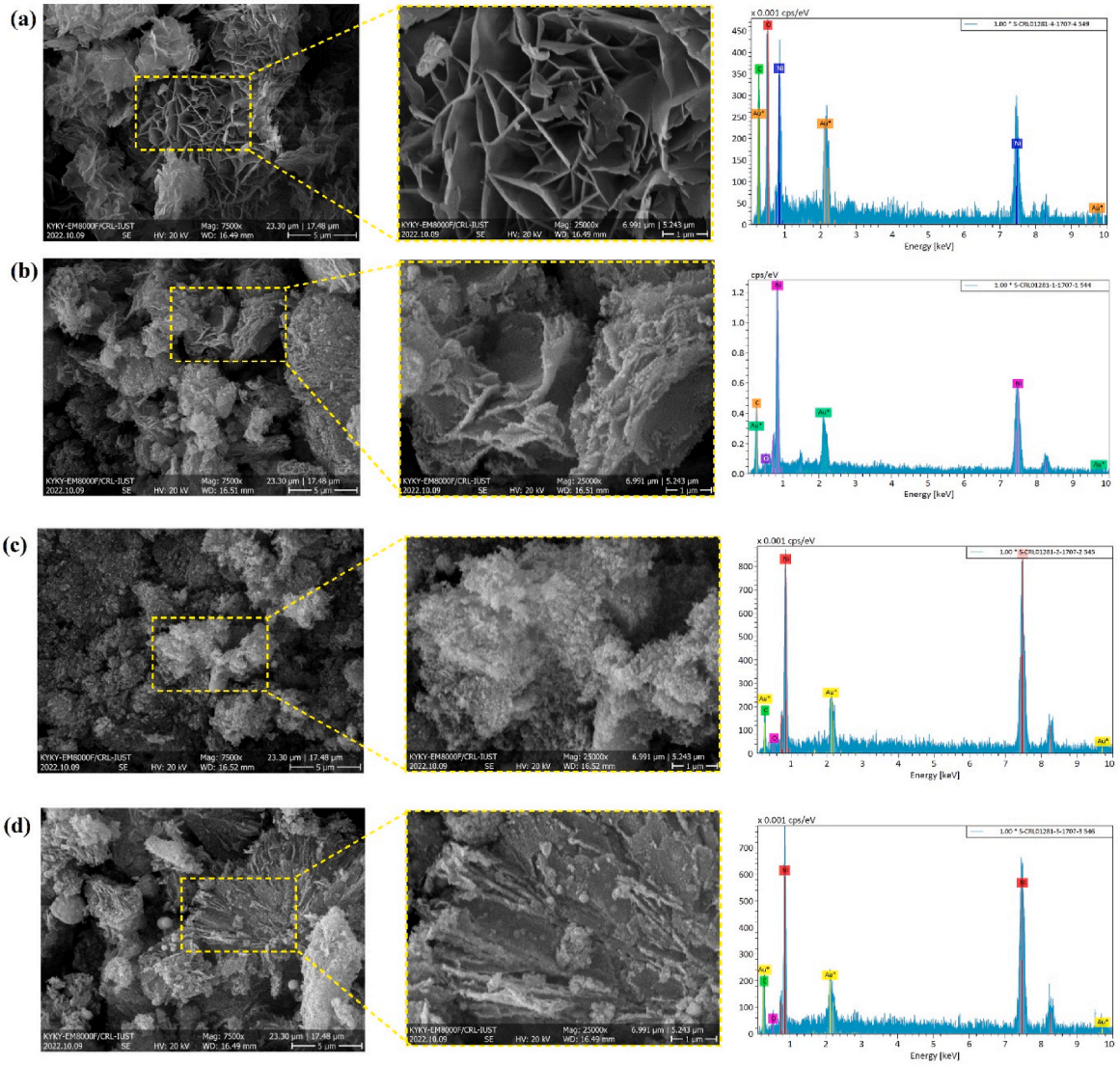

Fig. 3. FESEM images and EDX spectrum of (a) Ni-MOF and MOF-derived porous carbon nanocomposite at the temperature of (b) 700, (c) 800, and (d) 900 °C.

thickness in the range of 10–20 nm (Fig. 3(a)). On the other hand, MOF-derived porous carbon nanocomposites have different structures due to pyrolyzed processes at different temperatures. As it is obvious, with the increase in pyrolysis temperature, collapsing of the petal-shaped nanosheets has increased. Besides, the flower-like structure of the Ni-MOF has not changed significantly at 700 °C. But at higher temperatures, it has undergone noticeable changes (Fig. 3(b–d)). The elemental compositions of produced adsorbents were examined using X-ray energy dispersive spectroscopy, as shown in Fig. 3. Ni, O, and C are the three main components of EDX spectra. The higher amount of oxygen element than the other two elements in the Ni-MOF sample is clearly evident. However, after pyrolyzing, the oxygen peak is greatly reduced compared to nickel, and the main constituents of CDMs are nickel and carbon. These results are consistent with XRD observations.

As-prepared MOFs' textural features, such as total pore volume, mean pore diameter (at $P/P_0 = 0.980$), and specific surface area (a_s), have been investigated using the Brunauer-Emmett-Teller (BET) theory in the interpretation of N_2 adsorption-desorption isotherms. The findings are presented in Fig. 4. All as-synthesized samples (Ni-MOF and CDMs) exhibit type IV adsorption with H3 hysteresis loops, which is evident from the IUPAC classification and suggests that they all include mesopores (Sing and Williams, 2004) (Fig. 4(a)). Additionally, a substantial rise from capillary condensation may be observed at high relative pressure, which indicates the development of microporous (Yang and Bai, 2019). As a result, the fact that all as-synthesized samples have mesopores and macropores show that all created samples are hierarchical structures. Hysteresis loops occur as a consequence of irreversible adsorption and desorption (Zdravkov et al., 2007). Agglomerates of plate-like particles that create slot-shaped pores frequently exhibit H3 hysteresis, and the wider the slot-shaped pore, the greater the hysteresis loop is produced (Bohström and Lillerud, 2018; Tsai et al., 2008). It is clear from comparing the data reported in Table 1, pyrolyzing Ni-MOF greatly enhanced both the specific surface area and total pore volume. However, it can be observed that by increasing the pyrolysis temperature from 700 to 900 °C, the specific surface area and total pore volume have decreased from 103.94 m^2/g and 0.5401 cm^3/g to 60.015 m^2/g and 0.3127 cm^3/g, respectively. The mean pore volume has not significantly altered when the pyrolysis temperature has adjusted. Additionally, pore size irregularity is shown by an examination of the BJH adsorption-desorption pore distribution (Fig. 4(b)). The mesopore-microporous character of the samples' structure is shown by the fact that their pore size distribution falls between 1 and 50 nm.

Table 2 lists the magnetic characteristics, such as coercivity (H_c), saturation magnetization (M_s), and remnant magnetism (M_r). As it is clear from Fig. 5(a), the magnetization for Ni-MOF is close to zero, in other words, the fairly dominant paramagnetic signal can be clearly

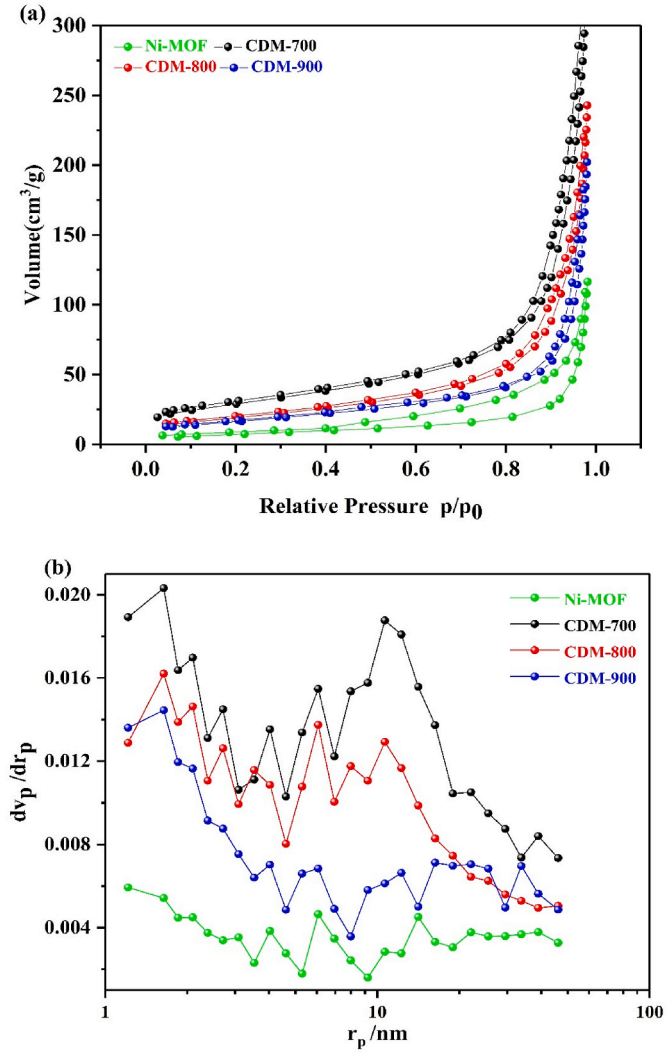

Fig. 4. (a) N_2 adsorption-desorption isotherms and (b) the distribution of BJH pore sizes.

Table 1
BET surface areas and pore properties of samples.

Sample	a_s (m^2/g)	Total pore volume (cm^3/g)	Mean pore diameter (nm)
Ni-MOF	27.23	0.1803	26.48
CDM-700	103.94	0.5401	20.79
CDM-800	68.81	0.3755	21.83
CDM-900	60.02	0.3127	20.84

Table 2
Magnetic characteristics of samples summarized.

Sample	M_s (emu/g)	M_r (emu/g)	H_c (Oe)
Ni-MOF	0.2320	0.0165	120.2722
CDM-700	32.6316	1.3294	10.8234
CDM-800	39.3099	3.6257	49.3518
CDM-900	42.0357	8.3594	88.6034

deduced in Ni-MOF. Magnetic hysteresis loops with a −10000 to 10,000 Oe range in the magnet field demonstrate that when the pyrolysis temperature rises from 700 to 900 °C, the saturation magnetization has increased by about 30%. Also, Fig. 5(b), which shows the magnified magnetic hysteresis loops in the field varying from −300 to 300 Oe, indicates that with the increase of pyrolysis temperature, H_c and M_r face similar changes to the values of M_s and have increased from 10.8234 Oe, 1.3294 emu/g to 88.6134 Oe and 8.3594 emu/g, respectively. This process, which results in the spontaneous generation of particles, is caused by surface spin disorder in the applied magnetic field (Shayesteh et al., 2021a). According to the research of Maya et al. some MOFs' metallic components unite to produce magnetic nanoparticles (MNPs) during the carbonization process, and the linkers, which turn into the key component of porous carbons, hold the MNPs (Maya et al., 2017). Metal ions can be changed into metal oxides by calcining the MOF at moderate temperatures, while other elements including nitrogen, carbon, and hydrogen can be oxidized to produce gaseous compounds. Consequently, oxides with linked holes are created as the gas is released during the calcination process. Because of their distinctive structure and significant surface area, MOFs are an ideal starting point for producing metal oxides (Xu et al., 2016). The magnetic property of synthesized samples is thus another noteworthy characteristic. Due to their speedy collection, ferromagnetic nickel particles will be advantageous in the removal process.

3.2. The effect of pyrolyze temperature

In the initial stage, the effect of different temperatures in pyrolysis has been depicted and the outcome is shown in Fig. 6. By comparing the adsorption capacity in 0.0025 and 0.001 g of mass adsorbent, it can be seen that the effect of pyrolysis was generally growing because CDM-900 has an adsorption capacity that is around three times more than Ni-MOF in both of these mass adsorbents. However, with increasing in pyrolysis temperature, as shown in FESEM analysis, the adsorption capacity was reduced as a result of the rise in clumping and reached from 552.6 to 1321.31 mg/g at 700 °C to 434.74 and 939.39 mg/g at 900 °C in 0.0025 and 0.001 g of mass adsorbent, respectively. When the pyrolysis temperature rises, less adsorption occurs as a result of a reduction in specific surface area and an increase in clumping, and CDM-700 represents maximum MO adsorption capacity, which is also proved by the results of N_2 adsorption-.desorption analysis. Caused by having the maximum adsorption capacity in both mass adsorbents, the MOF-derived porous carbon nanocomposite at the temperature of 700 °C (CDM-700) has been chosen to study other effective parameters on the adsorption capacity for MO removal.

3.2.1. Effect of adsorbent dosage

The effect of CDM-700 adsorbent dosage on the adsorption of MO dye is depicted in Fig. 7. It is evident that the rate of MO dye removal increased as the adsorbent dose increased, while the rate of dye removal afterward remains almost constant. For instance, when the adsorbent dose was raised from 0.033 to 1.66 g/L, the removal efficiency increased from 88 to 99.9%. The two elements contributing to the improved MO removal effectiveness are the growth of active adsorption sites and the presence of new active binding sites on the adsorbent surface (Liu et al., 2014). However, the unsaturated sites during adsorption have led to an increase in adsorption capacity with a decrease in dosage, which would need the usage of greater amounts of adsorbent to adsorb the dye molecules (Wanyonyi et al., 2014).

3.2.2. Effect of contact time

The changes in contact time have been examined as a factor to investigate various values of the methyl orange adsorption capacity by CDM-700 in order to estimate the adsorption equilibrium time. As a result, contact time ranging from 5 to 70 min was used to expose the adsorbent to our dye solution. According to the depiction in Fig. 8, the adsorption process started quickly but gradually slowed down over time. After 60 min, this process is fixed, and the process has reached the equilibrium time. The rate of adsorption is frequently rapid up until the equilibrium time due to the abundance of active sites. However, when the active sites become saturated beyond the equilibrium time, fewer molecules of methyl orange are adsorbed, and as a result, the adsorption

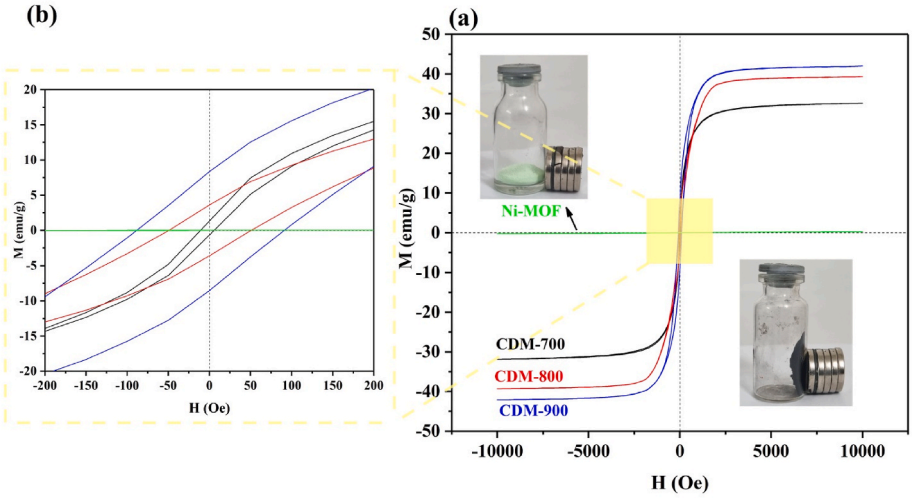

Fig. 5. Sample magnetic hysteresis (M–H) loops (a) and the enlarged magnetic hysteresis loops (b).

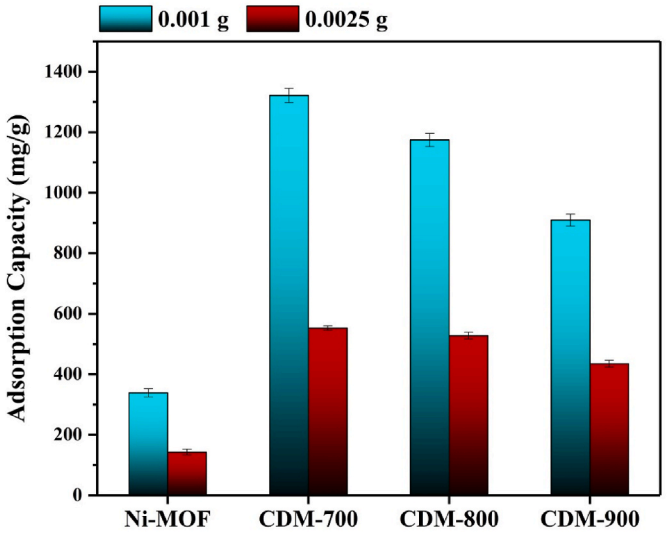

Fig. 6. MO adsorption and the pyrolyze temperature effect [initial MO concentration of 50 mg/L, volume of 30 mL, contact time of 60 min, feed pH of 6.4, and temperature of 25 °C].

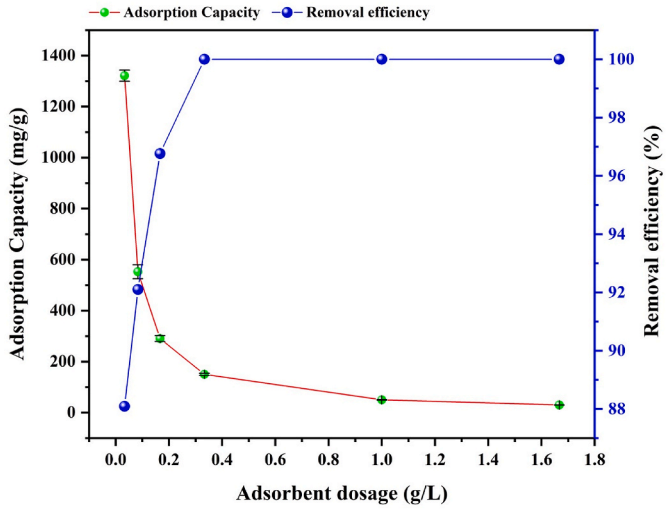

Fig. 7. Effect of adsorbent dosage on MO adsorption [initial MO concentration of 50 mg/L, volume of 30 mL, contact time of 60 min, feed pH of 6.4, and temperature of 25 °C].

capacity ceases (kheradmand et al., 2023).

3.2.2.1. Effect of solution pH. To reach the pH that corresponds to the point of zero charge (pH_{PZC}) of the adsorbent, you can use 0.01 M NaCl solutions with extra salt as the electrolyte (Sepehr et al., 2014). At first, the initial pH of a group of solutions containing 0.0025 g of adsorbent and 30 mL of electrolyte was adjusted using a pH meter (PL-500, EZDO, Taiwan), the solutions were then sonicated for 48 h, and finally after filtring of the suspensions, the adsorbent final pH was calculated. Next, pH_i is plotted against ΔpH ($\Delta pH = pH_f - pH_i$), and pH_{PZC} is obtained from the curve when ΔpH is zero. The pH_{PZC} adsorbent was equal to 5.2, as shown in Fig. 9.

The adsorption process was examined at various pH media of the sample solution to emphasize the important part that electrostatic interactions play (Fig. 10). It is evident that as the pH dropped from 5.2 to 3, MO adsorption increased dramatically. The positively charged adsorbent surface and the oppositely charged MO are drawn together by electrostatic attraction due to the anionic nature of methyl orange at pH less than 5.2, which is acidic due to the presence of H^+ (del Rio et al., 2022). As a result, the maximum adsorption capacity, measuring 574.68 mg/g at pH = 3, was found there. The adsorption capacity decreased at pH levels over pH_{zpc} as a result of the electrostatic repulsive between MO and oppositely charged surface sites and the conflict between extra OH^- and MO ions (Shayesteh et al., 2016). The lowest value of the adsorption capacity at pH = 12 with a value of 502.92 mg/g suggests the presence of additional interactions for dye adsorption, despite the fact that the data clearly demonstrate that electrostatic interactions play a significant part in the adsorption of the examined dye. Thus, MO adsorption continued in basic circumstances with increasing pH despite a decrease in adsorption capability compared to acidic conditions. Electrostatic and π-π interactions were significant in the removal of MO dye in addition to morphological characteristics, appropriate pores, and active adsorption sites.

3.2.3. Kinetic study

Reaction kinetic models to correctly understand the adsorption behavior uptake rate up to equilibrium were used. In general, the adsorption process includes the transfer of species from the solution to the solid surface, sorption on the surface, and finally the diffusion of the adsorbed molecules. The kinetics of the adsorption reaction provides important information about the adsorption rate, the mechanism gov-

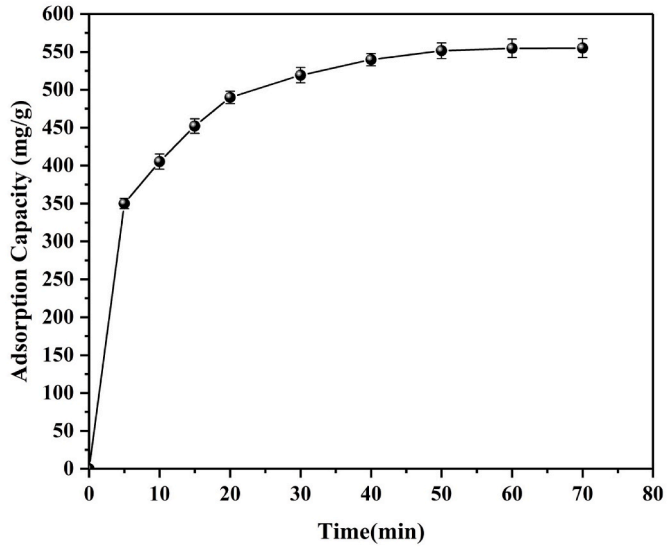

Fig. 8. MO adsorption and the contact time effect [initial MO concentration of 50, volume of 30 mL, feed pH of 6.4, adsorbent dosage of 0.083 g/L, temperature of 25 °C].

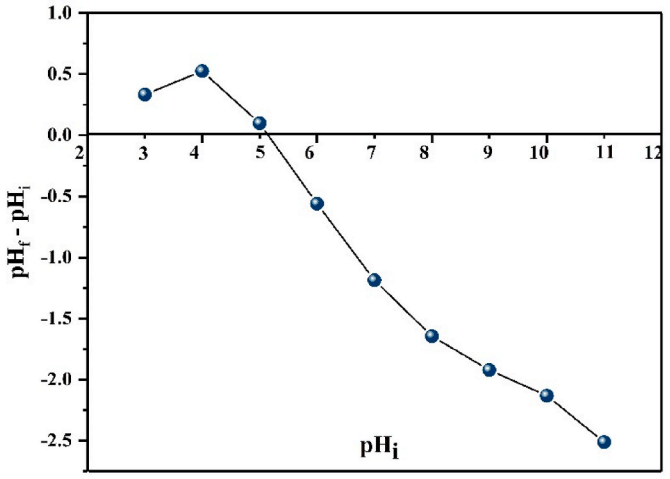

Fig. 9. Examining the point of zero charge [feed adsorbent dosage of 0.083 g/L, temperature of 25 °C, contact time of 48 h, and 125 rpm agitation speed].

erning the process, and the effectiveness of the adsorbent, which is useful in practical applications. Here, to identify the most appropriate kinetic model, the widely used nonlinear kinetic models, pseudo-first-order, pseudo-second-order, Elovich, and Fractional, were used to examine the changes in adsorption rate and fit the data, and the model equations are as Eqs. (3)–(6), respectively (kheradmand et al., 2023):

$$q_t = q_e\left(1 - e^{-k_1 t}\right) \tag{3}$$

$$q_t = \frac{k_2 q_e^2 t}{1 + k_2 q_e t} \tag{4}$$

$$q_t = \frac{1}{\beta} ln(\alpha\beta t + 1) \tag{5}$$

$$q_t = k_p t^{v_p} \tag{6}$$

In addition, the Weber–Morris intra-particle diffusion model to investigate the diffusion mechanism and the mass transfer process of MO onto the CDM-700 was applied. Its mathematic expression can be given as Eq.

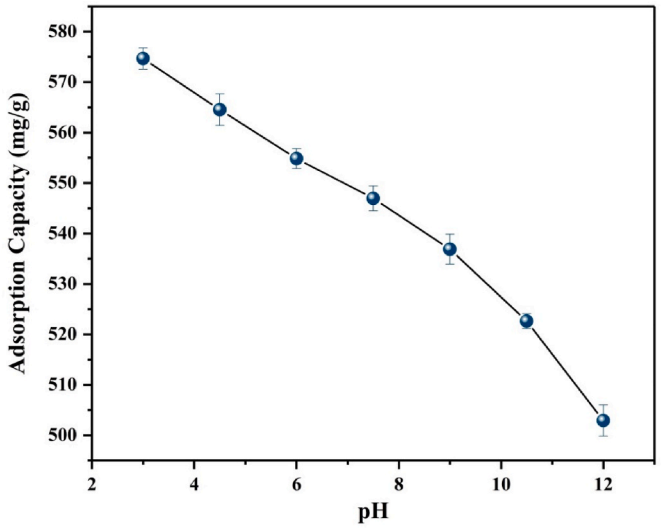

Fig. 10. MO adsorption and pH effects [initial MO concentration of 50 mg/L, volume of 30 mL, contact time of 60 min, adsorbent dosage of 0.083 g/L, and temperature of 25 °C].

(7) (Shayesteh et al., 2016):

$$q_t = k_{id} t^{1/2} + I \tag{7}$$

The values of the correlation coefficient (R^2) as well as the derivative of Marquardt's percent standard deviation (MPSD), the average relative error (ARE), and nonlinear chi-square test ($\chi 2$) tests were used to determine the best-fit models that were employed as following (Eqs. 8–10) (kheradmand et al., 2023):

$$MPSD = \sum_{i=1}^{n} \left[\left(\frac{q_{e,exap} - q_{e,calc}}{q_{e,calc}} \right)^2 \right]_i \tag{8}$$

$$ARE = \sum_{i=1}^{n} \left| \frac{\left(q_{e,\exp} - q_{e,calc}\right)}{q_{e,\exp}} \right|_i \tag{9}$$

$$\chi^2 = \sum_{i=1}^{n} \left[\frac{\left(q_{e,exap} - q_{e,calc}\right)^2}{q_{e,calc}} \right]_i \tag{10}$$

The fitting results of the non-linearized kinetic models are shown in

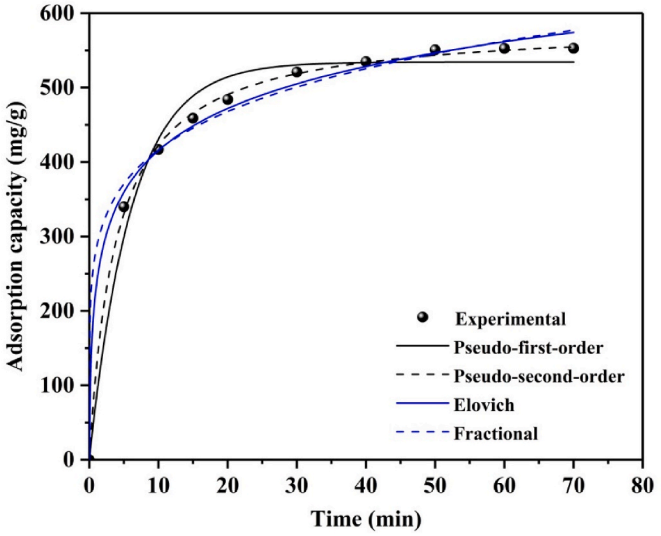

Fig. 11. Non-linear kinetic plots for MO dye onto CDM-700.

Fig. 11, and the variables are listed in Table 3. The pseudo-second-order model has an adsorption capacity that is most comparable to the results of the experiments, and its correlation coefficient is higher than other models. The pseudo-second-order model can be applied to the adsorption of MO onto the CDM-700 because its derivative of Marquardt's percent standard deviation, the average relative error, and nonlinear chi-square tests were lower compared to the other models. Therefore, the pseudo-second-order model is more appropriate for simulating the kinetic adsorption process and proving the occurrence of MO chemisorption on CDM-700.

Fig. 12 displays the linear Weber-Morris intra-particle diffusion model plot. The finding of three distinct linear parts suggests that the MO dye adsorption on the CDM takes place over the course of three steps. The first, sharper section is responsible for adsorbate diffusion through the solution to the adsorbent exterior surface or boundary layer diffusion of solute molecules. The gradual equilibrium stage, which is dominated by intra-particle diffusion, makes up the second linear component. The third section is attributed to the final equilibrium stage when intra-particle diffusion began to slow down as a result of the incredibly low adsorbate concentration still present in the solution. Intra-particle diffusion is not the only phase that is rate-limiting in the MO dye sorption process on CDM-700, as shown by the fact that none of the three linear sections of the Weber-Morris intra-particle diffusion model passed through the coordinate origin. As a result, the MO adsorption processes involve both intra-particle diffusion and boundary layer diffusion. Table 4 shows that the k_{id} values are in the following order: $k_{1d} > k_{2d} > k_{3d}$. This indicates that there has been little intra-particle diffusion and a significant transfer of dye from the solution to the external surface of the adsorbent, likely as a result of the quick formation of multilayers, up until the concentration of adsorbate in solution decreases. It was clear that none of the three phases had simplex intra-particle diffusion because none of the I_1, I_2, or I_3 values were equal to zero.

3.2.4. Isotherm study

Different initial MO concentrations (10–1000 mg/L) were applied to the adsorbents to evaluate their adsorption capacity. Due to the large number of vacant active sites, the results show a substantial and rising adsorption speed. However, the adsorption process comes to an equilibrium and the active sites are saturated, causing the adsorption rate to decrease. This is because of the fact that the adsorbate molecules or ions enhance the driving force at larger concentrations due to the increase in the concentration of the pressure gradient and hasten the mass transfer between the liquid adsorbate and solid adsorbent. As a result, the adsorption speed is improved at higher initial concentrations of methyl orange. Finally, due to a lack of active sites, adsorption approaches equilibrium. For carbon-derived adsorbents, raising the MO concentration can be enhanced the adsorption capacity. One of the most significant causes of the occurrence is the rise in the specific surface of the adsorbent during pyrolysis.

Table 3
Kinetic variables for MO adsorption on CDM-700.

Kinetic model	Parameters	Value
Experimental	$q_{e,exp}$	552.72
Pseudo-first-order	$q_{e,cal}$ (mg/g)	534.33
	k_1 (1/min)	0.1642
	R^2	0.9819
	χ^2	11.5714
	MPSD	0.0305
	ARE	0.4088
Pseudo-second-order	$q_{e,cal}$ (mg/g)	585.45
	k_2 (g/mg × min)	0.0004
	R^2	0.9989
	χ^2	0.6658
	MPSD	0.0016
	ARE	0.0980
Elovich	α	1313.19
	β	0.0122
	R^2	0.9943
	χ^2	3.1539
	MPSD	0.0559
	ARE	0.5848
Fractional	k_p	282.9618
	v_p	0.1678
	R^2	0.9899
	χ^2	5.7375
	MPSD	0.0131
	ARE	0.2752

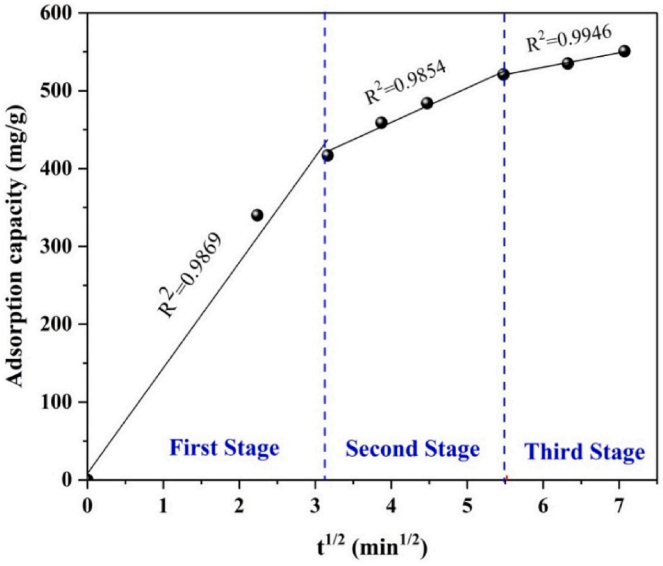

Fig. 12. Weber-Morris intra-particle diffusion model for removing MO adsorption by CDM-700.

The results of equilibrium are essential for defining adsorption because an exact description of the separation of liquid and solid phases to equilibrium is required to comprehend the adsorption of adsorbed molecules from the liquid medium to the sorbent surface. Five well-known non-linear mathematical models—Langmuir, Freundlich, Temkin, Jovanovic, and Halsey—were fitted to the MO dye adsorption data on Ni-MOF, CDM-700, CDM-800, and CDM-900, which are each described by Eqs. 11–15 (kheradmand et al., 2023; Shayesteh et al., 2021b):

$$q_e = \frac{q_m K_L C_e}{1 + K_L C_e} \tag{11}$$

$$q_e = K_F C_e^{1/n} \tag{12}$$

$$q_e = \left(\frac{RT}{b_T}\right) \ln\left(K_T C_e\right) \tag{13}$$

$$q_e = q_{mj}\left(1 - e^{\left(K_j C_e\right)}\right) \tag{14}$$

$$q_e = \exp\left(\frac{ln\, K_H - ln\, C_e}{n}\right) \tag{15}$$

The non-linear isotherms for the five models for Ni-MOF, CDM-700, CDM-800, and CDM-900 are shown in Fig. 13. The values of various constants, fitting information, including various error analyses, and the correlation coefficient R^2 for all isotherm models are all included in Table 5. The model with the highest correlation to the experimental data is identified using the calculated correlation coefficient and error analysis value. Based on the estimated data from the various models of the two-parameter isotherms, the correlation coefficients of Langmuir are larger than the values for the other four isotherms. Furthermore, the

Table 4
Weber-Morris intra-particle diffusion model constants to remove MO by CDM-700.

First adsorption stage			Second adsorption stage			Third adsorption stage		
k_{1d} (mg g^{-1} min$^{-1/2}$)	I_1	R_1^2	k_{2d} (mg g^{-1} min$^{-1/2}$)	I_2	R_2^2	k_{3d} (mg g^{-1} min$^{-1/2}$)	I_3	R_3^2
135.56	8.3449	0.9869	44.28	282.12	0.9854	18.62	418.33	0.9946

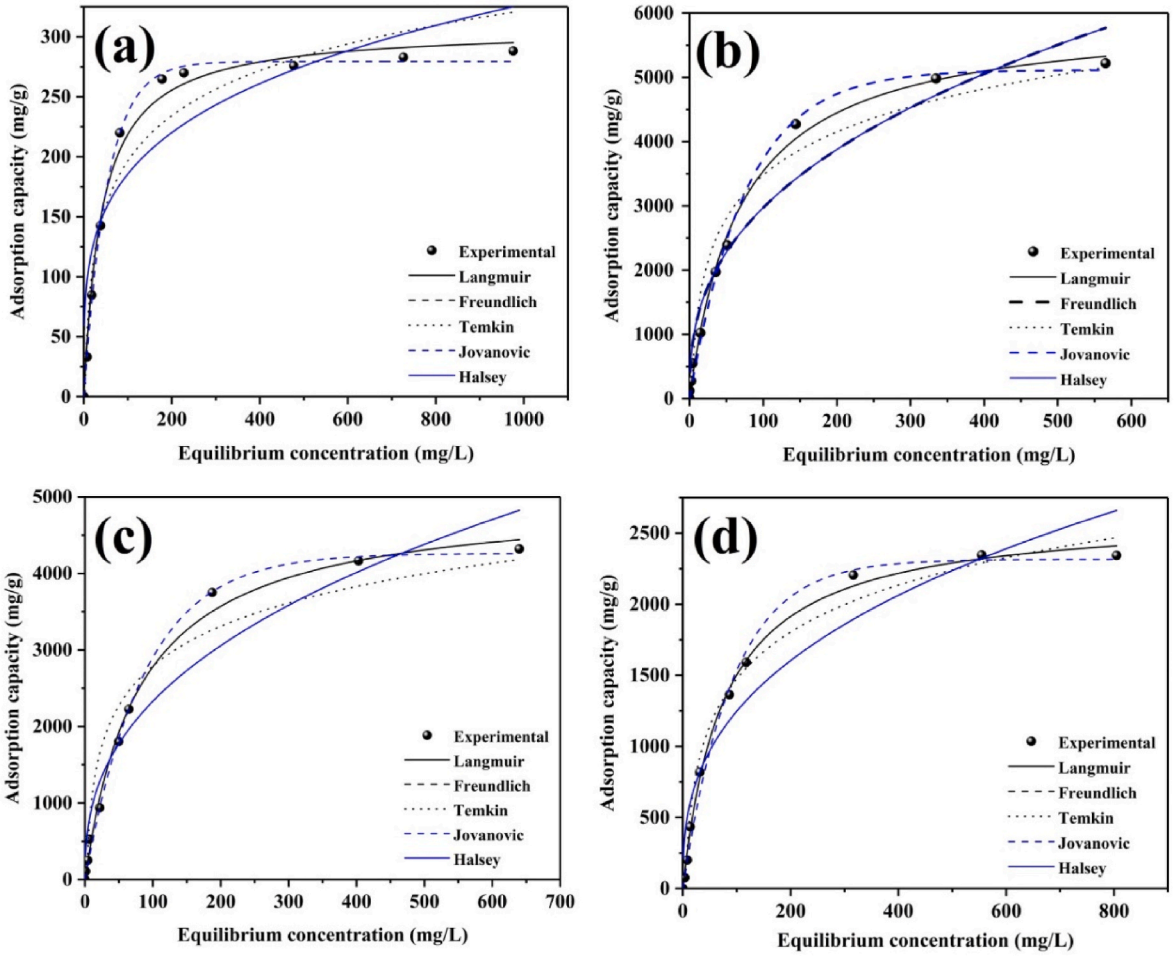

Fig. 13. Non-linear adsorption isotherm plots for (a) MOF (Ni), (b) CDM-700, (c) CDM-800, and (d) CDM-900.

error analysis value for it is the lowest. Thus, compared to the other four models, the Langmuir model more closely matches the data. This outcome demonstrates that monolayer sorption took place on a homogeneous surface during the adsorption process. In addition, Table 6 shows comparisons between the effectiveness of various materials for adsorption of MO and that of the prepared adsorbents. The adsorption performance of carbon-derived adsorbents is superior to that of other composites described in the literature. Its larger surface area and distinctive morphology may account for its enhanced adsorption capacity. Based on the comparison, carbon-derived adsorbent has a strong capacity for removing MO from an aqueous medium and may be used as an effective adsorbent.

3.2.4.1. Reusability. Easy regeneration and great recyclability are two of the most significant effective factors for the efficacy of various adsorbents in practical applications. An ideal adsorbent should not only have a high adsorption capacity, but it should also retain part of that capacity in subsequent adsorption-desorption cycles. Therefore, to investigate the regeneration of the adsorbent, the solvent elution method was used with the help of ethanol due to its higher solubility for MO. The results of five consecutive experiments on MO adsorption for CDM-700 are shown in Fig. 14. As it is known, with the increase of regeneration cycles, the calculated adsorption capacity after 5 cycles of adsorption and desorption has decreased to 1010.45 and 359.89 mg/g for 0.001 and 0.0025 g, respectively, which shows the reusability and satisfactory stability. Hence, it can be suggested that CDMs can act as a recyclable adsorbent.

3.2.5. Effects of coexisting ions

The presence of dissolved common ions in water can significantly influence the adsorption process during wastewater treatment. This is an essential consideration when comparing the efficacy of various adsorbent materials. In practical applications, material suitability is of paramount importance. Therefore, the impact of coexisting various ions such as Na^+, K^+, Ca^{2+}, No_3^-, HPO_4^-, and Cl^- (1 mol/L) on the adsorption capacity of CDM-700 was evaluated, and the results were shown in Fig. 15. Despite the presence of these ions, the results indicated that CDM-700 had a significant adsorption capacity and was capable of removing dyes from effluent. Therefore, CDM-700 could be utilized as an adsorbent in industrial effluent treatment applications. The results

Table 5
Comparison of the model parameters for MO adsorption onto the adsorbents.

Isotherm model	Parameter	Ni-MOF	CDM-700	CDM-800	CDM-900
Langmuir	q_{max} (mg/g)	307.38	5976.35	4992.39	2636.54
	K_L (L/mg)	0.0247	0.0146	0.0126	0.0133
	R^2	0.9913	0.9956	0.9948	0.9974
	χ^2	7.8868	239.9359	162.3802	41.0308
	MPSD	0.1909	0.3033	0.3084	0.4674
	ARE	0.7976	0.9709	1.0995	1.1287
Freundlich	K_F (mg/g)/(mg/L)^n	59.86	509.82	382.46	234.05
	n	4.0680	2.6114	2.5487	2.7525
	R^2	0.8796	0.9594	0.9493	0.9374
	χ^2	89.9059	749.6724	913.1762	640.7805
	MPSD	4.0775	2.6875	9.7340	18.0383
	ARE	3.1589	2.8363	5.5216	6.4314
Temkin	b_T	45.54	2.56	3.31	5.20
	K_T (L/g)	0.3710	0.3661	0.4163	0.2210
	R^2	0.9497	0.9618	0.9353	0.9861
	χ^2	1155.0331	1804.9540	937.5546	930.8354
	MPSD	0.3896	3.8253	41.5762	5.0123
	ARE	1.3944	3.3540	8.2132	3.1213
Jovanovic	q_{mj}	279.45	5115.19	4261.46	2315.82
	K_j	−0.0188	−0.0131	−0.0115	−0.0109
	R^2	0.9984	0.9954	0.9972	0.9944
	χ^2	1.0106	496.8115	298.1473	79.0370
	MPSD	0.0106	0.5462	0.5620	0.1398
	ARE	0.2291	1.2771	1.3040	0.7689
Halsey	K_H	5.82E-08	8.40E-08	2.58E-07	2.98E-07
	n	−4.0704	−2.6130	−2.5506	−2.7540
	R^2	0.8796	0.9594	0.9493	0.9374
	χ^2	89.9327	750.8047	914.7045	641.2540
	MPSD	4.0843	2.6980	9.7778	18.0783
	ARE	3.1610	2.8414	5.5324	6.4383

Table 6
Maximum MO adsorption capacity comparison with different adsorbents.

Adsorbent	Adsorption capacity (mg/g)	Ref.
Cetyltrimethylammonium bromide modified pumice	31.73	Shayesteh et al. (2021b)
Chitosan microspheres	207	Zhai et al. (2018)
Lapindo volcanic mud (LVM)	333.3	Jalil et al. (2010)
ZIF-8	183	Lei et al. (2023)
ZIF-8@polyethyleneimine-cyanuric chloride	710	Lei et al. (2023)
Waste-cellulose-derived porous carbon	337.8	Sun et al. (2019)
Coffee grounds Activated Carbon	658	Rattanapan et al. (2017)
UiO-66-NH_2	28.97	Chen et al. (2015)
Commercial activated carbon	113.63	Khattabi et al. (2021)
UiO-66	233.65	Molavi et al. (2018)
CTAB-hectorite	567.26	Asranudin et al. (2022)
Activated clay	16.78	Ma et al. (2013)
Banana peel	21.0	Annadurai et al. (2002)
Modified wheat straw	50.4	Su et al. (2014)
Lemon peels-derived activated carbon	33	Ramutshatsha-Makhwedzha et al. (2022)
Ni-based metal-organic framework (Ni-MOF)	307.38	Present study
Ni/C-derived from MOF (Ni) at 700 °C (CDM-700)	5976.35	Present study
Ni/C-derived from MOF (Ni) at 800 °C (CDM-800)	4992.39	Present study
Ni/C-derived from MOF (Ni) at 900 °C (CDM-900)	2636.54	Present study

indicate that the presence of common ions in drinking water has little influence on the efficacy of CDM-700 as an adsorbent. These results have significant implications for the design and development of efficient

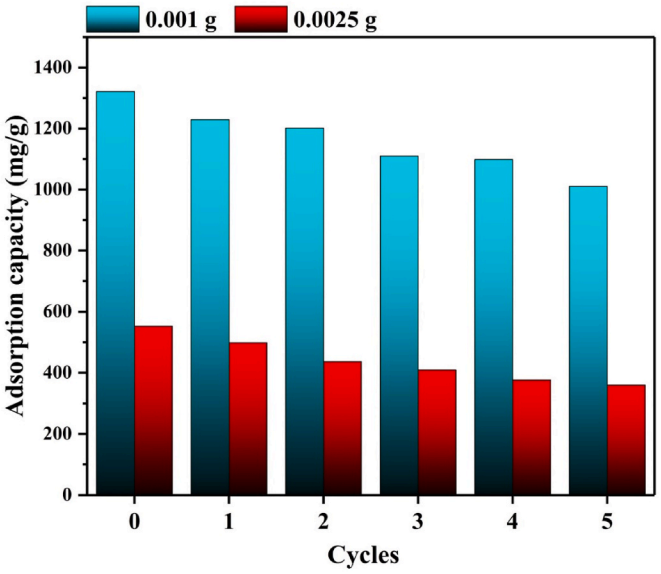

Fig. 14. Regeneration studies of prepared CDM-700 for MO dye.

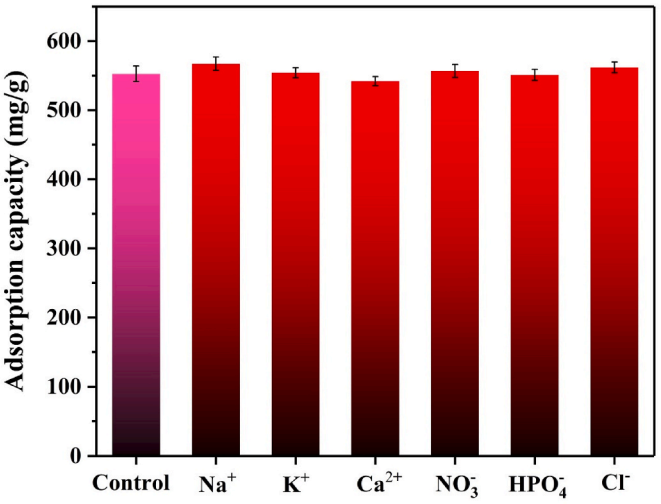

Fig. 15. Effect of coexisting ions on MO adsorption [initial MO concentration of 50 mg/L, volume of 30 mL, contact time of 60 min, feed pH of 6.4, adsorbent dosage of 0.0833 g/L, and temperature of 25 °C].

wastewater treatment technologies that can remove pollutants and other contaminants from wastewater streams.

4. Conclusion

In summary, a straightforward solvothermal route was used to produce petal-shaped Ni-MOF nanosheets. Following, the as-prepared Ni-MOF was pyrolyzed under an inert atmosphere (N_2) at temperatures of 700, 800, and 900 °C to obtain magnetic porous carbons. The adsorption rate of the methyl orange dye was used to compare the performance of the synthetic MOF and pyrolyzed magnetic nanocomposites. Due to its high surface area (103.94 m^2/g) and overall pore volume (0.5401 cm^3/g), CDM-700 was found to have the highest adsorption capacity (5976.35 mg/g). Electrostatic and π-π interactions were significant in the removal of MO dye in addition to morphological characteristics, appropriate pores, and active adsorption sites. The ability to adsorb the adsorbent from water samples by using simply an external magnetic field is another benefit of the magnetic nanocomposite. By effectively

reusing CDM-700 over five adsorption-desorption cycles, this approach also benefits from the minimal consumption of organic solvent and nanosorbent and its environmental friendliness. The pseudo-second-order and intra-particle diffusion model which is proposed by Weber and Morris are more effective at explaining the kinetics of the produced adsorbents. The performance of the Langmuir model in fitting the experimental data was better than the models developed by Freundlich, Temkin, Halsey, and Jovanovic for fitting the equilibrium isotherm. The development of a superadsorbent for wastewater treatment resulted from the understanding of the impact of various pyrolysis temperatures in Ni-MOF provided. Finally, it should be highlighted that the discovered approach can be used to produce more porous carbons with innovative forms and qualities that have enormous potential in a variety of fields.

Credit authorn statement

Negar Beigi: Experimental work, Methodology, Data curation, Software, Formal analysis, Investigation, Writing – original draft, Writing – review & editing.; **Hadi Shayesteh**: Conceptualization, Methodology, Software, Conceived and designed the experiments, Resources, Writing – original draft, Writing – review & editing, Visualization.; **Shahrzad Javanshir**: Supervision, Conceptualization, Methodology.; **Majid Hosseinzadeh**: Supervision, Conceptualization, Funding acquisition, Methodology, Validation, Resources, Data curation, Review & editing, Supervision.

Declaration of competing interest

The authors declare that they have no known competing financial interests or personal relationships that could have appeared to influence the work reported in this paper.

Data availability

No data was used for the research described in the article.

Appendix A. Supplementary data

Supplementary data to this article can be found online at https://doi.org/10.1016/j.envres.2023.116146.

References

Ahmad, K., Nazir, M.A., Qureshi, A.K., Hussain, E., Najam, T., Javed, M.S., Shah, S.S.A., Tufail, M.K., Hussain, S., Khan, N.A., Shah, H.-R., Ashfaq, M., 2020. Engineering of Zirconium based metal-organic frameworks (Zr-MOFs) as efficient adsorbents. Mater. Sci. Eng. B 262, 114766. https://doi.org/10.1016/j.mseb.2020.114766.

Ahmad, K., Shah, H.-R., Ashfaq, M., Shah, S.S.A., Hussain, E., Naseem, H.A., Parveen, S., Ayub, A., 2021. Effect of metal atom in zeolitic imidazolate frameworks (ZIF-8 & 67) for removal of Pb2+ & Hg2+ from water. Food Chem. Toxicol. 149, 112008 https://doi.org/10.1016/j.fct.2021.112008.

Alsbaiee, A., Smith, B.J., Xiao, L., Ling, Y., Helbling, D.E., Dichtel, W.R., 2016. Rapid removal of organic micropollutants from water by a porous β-cyclodextrin polymer. Nature 529, 190–194. https://doi.org/10.1038/nature16185.

Annadurai, G., Juang, R.S., Lee, D.J., 2002. Use of cellulose-based wastes for adsorption of dyes from aqueous solutions. J. Hazard Mater. 92, 263–274. https://doi.org/10.1016/S0304-3894(02)00017-1.

Arslan, İ., Balcioğlu, I.A., Bahnemann, D.W., 2000. Advanced chemical oxidation of reactive dyes in simulated dyehouse effluents by ferrioxalate-Fenton/UV-A and TiO2/UV-A processes. Dyes Pigments 47, 207–218. https://doi.org/10.1016/S0143-7208(00)00082-6.

Asgharinezhad, A.A., Ebrahimzadeh, H., 2021. Magnetic porous carbon nanocomposite derived from cobalt based-metal-organic framework for extraction and determination of homo and hetero-polycyclic aromatic hydrocarbons. Talanta 233, 122526. https://doi.org/10.1016/j.talanta.2021.122526.

Asranudin, Purnomo, A.S., Prasetyoko, D., Bahruji, H., Holilah, 2022. Single-step synthesis and modification of CTAB-hectorite for efficient adsorption of methyl orange dye. Mater. Chem. Phys. 291, 126749 https://doi.org/10.1016/j.matchemphys.2022.126749.

Bohström, Z., Lillerud, K.P., 2018. Preparation of chabazite with mesopores templated from a cationic polymer. Microporous Mesoporous Mater. 271, 295–300. https://doi.org/10.1016/j.micromeso.2018.05.049.

Cabrita, I., Ruiz, B., Mestre, A.S., Fonseca, I.M., Carvalho, A.P., Ania, C.O., 2010. Removal of an analgesic using activated carbons prepared from urban and industrial residues. Chem. Eng. J. 163, 249–255. https://doi.org/10.1016/j.cej.2010.07.058.

Chen, M., Chen, J., Liu, Y., Liu, J., Li, L., Yang, B., Ma, L., 2019. Enhanced adsorption of thiophene with the GO-modified bimetallic organic framework Ni-MOF-199. Colloids Surfaces A Physicochem. Eng. Asp. 578, 123553 https://doi.org/10.1016/j.colsurfa.2019.06.019.

Chen, Q., He, Q., Lv, M., Xu, Y., Yang, H., Liu, X., Wei, F., 2015. Selective adsorption of cationic dyes by UiO-66-NH2. Appl. Surf. Sci. 327, 77–85.

Chin, M., Cisneros, C., Araiza, S.M., Vargas, K.M., Ishihara, K.M., Tian, F., 2018. Rhodamine B degradation by nanosized zeolitic imidazolate framework-8 (ZIF-8). RSC Adv. 8, 26987–26997. https://doi.org/10.1039/C8RA03459A.

Costa, J.A.S., de Jesus, R.A., Santos, D.O., Mano, J.F., Romão, L.P.C., Paranhos, C.M., 2020. Recent progresses in the adsorption of organic, inorganic, and gas compounds by MCM-41-based mesoporous materials. Microporous Mesoporous Mater. 291, 109698 https://doi.org/10.1016/j.micromeso.2019.109698.

Dai, Y., Zhang, N., Xing, C., Cui, Q., Sun, Q., 2019. The adsorption, regeneration and engineering applications of biochar for removal organic pollutants: a review. Chemosphere 223, 12–27. https://doi.org/10.1016/j.chemosphere.2019.01.161.

del Rio, M., Grimalt Escarabajal, J.C., Turnes Palomino, G., Palomino Cabello, C., 2022. Zinc/Iron mixed-metal MOF-74 derived magnetic carbon nanorods for the enhanced removal of organic pollutants from water. Chem. Eng. J. 428, 131147 https://doi.org/10.1016/j.cej.2021.131147.

Dhaka, S., Kumar, R., Deep, A., Kurade, M.B., Ji, S.-W., Jeon, B.-H., 2019. Metal–organic frameworks (MOFs) for the removal of emerging contaminants from aquatic environments. Coord. Chem. Rev. 380, 330–352. https://doi.org/10.1016/j.ccr.2018.10.003.

Eluri, R., Paul, B., 2012. Synthesis of nickel nanoparticles by hydrazine reduction: mechanistic study and continuous flow synthesis. J. Nanoparticle Res. 14, 800. https://doi.org/10.1007/s11051-012-0800-1.

Gan, L., Wang, L., Xu, L., Fang, X., Pei, C., Wu, Y., Lu, H., Han, S., Cui, J., Shi, J., Mei, C., 2021. Fe3C-porous carbon derived from Fe2O3 loaded MOF-74 (Zn) for the removal of high concentration BPA : the integrations of adsorptive/catalytic synergies and radical/non-radical mechanisms. J. Hazard Mater. 413, 125305 https://doi.org/10.1016/j.jhazmat.2021.125305.

Hasan, Z., Jhung, S.H., 2015. Removal of hazardous organics from water using metal-organic frameworks (MOFs): plausible mechanisms for selective adsorptions. J. Hazard Mater. 283, 329–339. https://doi.org/10.1016/j.jhazmat.2014.09.046.

Hemmati, F., Norouzbeigi, R., Sarbisheh, F., Shayesteh, H., 2016. Malachite green removal using modified sphagnum peat moss as a low-cost biosorbent: kinetic, equilibrium and thermodynamic studies. J. Taiwan Inst. Chem. Eng. 58, 482–489. https://doi.org/10.1016/j.jtice.2015.07.004.

Huang, Q., Chai, K., Zhou, L., Ji, H., 2020. A phenyl-rich β-cyclodextrin porous crosslinked polymer for efficient removal of aromatic pollutants: insight into adsorption performance and mechanism. Chem. Eng. J. 387 https://doi.org/10.1016/j.cej.2020.124020.

Hussain, S., Javed, M.S., Asim, S., Shaheen, A., Khan, A.J., Abbas, Y., Ullah, N., Iqbal, A., Wang, M., Qiao, G., Yun, S., 2020. Novel gravel-like NiMoO4 nanoparticles on carbon cloth for outstanding supercapacitor applications. Ceram. Int. 46, 6406–6412. https://doi.org/10.1016/j.ceramint.2019.11.118.

Jalil, A.A., Triwahyono, S., Adam, S.H., Rahim, N.D., Aziz, M.A.A., Hairom, N.H.H., Razali, N.A.M., Abidin, M.A.Z., Mohamadiah, M.K.A., 2010. Adsorption of methyl orange from aqueous solution onto calcined Lapindo volcanic mud. J. Hazard Mater. 181, 755–762.

Jiang, N., Shang, R., Heijman, S.G.J., Rietveld, L.C., 2018. High-silica zeolites for adsorption of organic micro-pollutants in water treatment: a review. Water Res. 144, 145–161. https://doi.org/10.1016/j.watres.2018.07.017.

Khan, N.A., Shaheen, S., Najam, T., Shah, S.S.A., Javed, M.S., Nazir, M.A., Hussain, E., Shaheen, A., Hussain, S., Ashfaq, M., 2021. Efficient removal of norfloxacin by MOF@GO composite: isothermal, kinetic, statistical, and mechanistic study. Toxin Rev. 40, 915–927. https://doi.org/10.1080/15569543.2020.1801750.

Khattabi, E.H., Rachdi, Y., Bassam, R., Mourid, E.H., Naimi, Y., Alouani, M., Belaaouad, S., 2021. Enhanced elimination of methyl orange and recycling of an eco-friendly adsorbent activated carbon from aqueous solution. Russ. J. Phys. Chem. B 15, S149–S159.

kheradmand, A., Negarestani, M., Kazemi, S., Shayesteh, H., Javanshir, S., Ghiasinejad, H., Jamshidi, E., 2023. Design and preparation magnetic bio-surfactant rhamnolipid-layered double hydroxide nanocomposite as an efficient and recyclable adsorbent for the removal of Rifampin from aqueous solution. Sep. Purif. Technol. 304, 122362 https://doi.org/10.1016/j.seppur.2022.122362.

Kim, J.W., Ki, C.S., Um, I.C., Park, Y.H., 2017. A facile fabrication method and the boosted adsorption and photodegradation activity of CuO nanoparticles synthesized using a silk fibroin template. J. Ind. Eng. Chem. 56, 335–341. https://doi.org/10.1016/j.jiec.2017.07.029.

Lazaridis, N.K., Karapantsios, T.D., Georgantas, D., 2003. Kinetic analysis for the removal of a reactive dye from aqueous solution onto hydrotalcite by adsorption. Water Res. 37, 3023–3033. https://doi.org/10.1016/S0043-1354(03)00121-0.

Lei, Y., Liu, X., Zhang, J., Dai, Z., Zhao, X., Liu, G., 2023. A novel composite (ZIF-8@PEI-CC) with enhanced adsorption capacity and kinetics of methyl orange. J. Solid State Chem. 318, 123758 https://doi.org/10.1016/j.jssc.2022.123758.

Liu, S., Ding, Y., Li, P., Diao, K., Tan, X., Lei, F., Zhan, Y., Li, Q., Huang, B., Huang, Z., 2014. Adsorption of the anionic dye Congo red from aqueous solution onto natural

zeolites modified with N,N-dimethyl dehydroabietylamine oxide. Chem. Eng. J. 248, 135–144. https://doi.org/10.1016/j.cej.2014.03.026.
Lu, H., Zhang, L., Wang, B., Long, Y., Zhang, M., Ma, J., Khan, A., Chowdhury, S.P., Zhou, X., Ni, Y., 2019. Cellulose-supported magnetic Fe3O4–MOF composites for enhanced dye removal application. Cellulose 26, 4909–4920. https://doi.org/10.1007/s10570-019-02415-y.
Lu, W., Wu, X., 2018. Ni-MOF nanosheet arrays: efficient non-noble-metal electrocatalysts for non-enzymatic monosaccharide sensing. New J. Chem. 42, 3180–3183. https://doi.org/10.1039/C7NJ04754A.
Ma, Q., Shen, F., Lu, X., Bao, W., Ma, H., 2013. Studies on the adsorption behavior of methyl orange from dye wastewater onto activated clay. Desalination Water Treat. 51, 3700–3709. https://doi.org/10.1080/19443994.2013.782083.
Majano, G., Pérez-Ramírez, J., 2013. Scalable room-temperature conversion of copper(II) hydroxide into HKUST-1 (Cu3(btc)2). Adv. Mater. 25, 1052–1057. https://doi.org/10.1002/adma.201203664.
Maya, F., Palomino Cabello, C., Frizzarin, R.M., Estela, J.M., Turnes Palomino, G., Cerdà, V., 2017. Magnetic solid-phase extraction using metal-organic frameworks (MOFs) and their derived carbons. TrAC, Trends Anal. Chem. 90, 142–152. https://doi.org/10.1016/j.trac.2017.03.004.
Molavi, H., Hakimian, A., Shojaei, A., Raeiszadeh, M., 2018. Selective dye adsorption by highly water stable metal-organic framework: long term stability analysis in aqueous media. Appl. Surf. Sci. 445, 424–436.
Najam, T., Ahmad Shah, S.S., Ding, W., Deng, J., Wei, Z., 2019. Enhancing by nano-engineering: hierarchical architectures as oxygen reduction/evolution reactions for zinc-air batteries. J. Power Sources 438, 226919. https://doi.org/10.1016/j.jpowsour.2019.226919.
Nazir, M.A., Bashir, M.A., Najam, T., Javed, M.S., Suleman, S., Hussain, S., Kumar, O.P., Shah, S.S.A., Rehman, A. ur, 2021a. Combining structurally ordered intermetallic nodes: kinetic and isothermal studies for removal of malachite green and methyl orange with mechanistic aspects. Microchem. J. 164, 105973 https://doi.org/10.1016/j.microc.2021.105973.
Nazir, M.A., Najam, T., Zarin, K., Shahzad, K., Javed, M.S., Jamshaid, M., Bashir, M.A., Shah, S.S.A., Rehman, A.U., 2021b. Enhanced adsorption removal of methyl orange from water by porous bimetallic Ni/Co MOF composite: a systematic study of adsorption kinetics. Int. J. Environ. Anal. Chem. 00, 1–16. https://doi.org/10.1080/03067319.2021.1931855.
Neisi, Z., Ansari-Asl, Z., Jafarinejad-Farsangi, S., Tarzi, M.E., Sedaghat, T., Nobakht, V., 2019. Synthesis, characterization and biocompatibility of polypyrrole/Cu(II) metal-organic framework nanocomposites. Colloids Surf. B Biointerfaces 178, 365–376. https://doi.org/10.1016/j.colsurfb.2019.03.032.
Pacheco-Álvarez, M.O.A., Picos, A., Pérez-Segura, T., Peralta-Hernández, J.M., 2019. Proposal for highly efficient electrochemical discoloration and degradation of azo dyes with parallel arrangement electrodes. J. Electroanal. Chem. 838, 195–203. https://doi.org/10.1016/j.jelechem.2019.03.004.
Ramutshatsha-Makhwedzha, D., Mavhungu, A., Moropeng, M.L., Mbaya, R., 2022. Activated carbon derived from waste orange and lemon peels for the adsorption of methyl orange and methylene blue dyes from wastewater. Heliyon 8, e09930. https://doi.org/10.1016/j.heliyon.2022.e09930.
Rattanapan, S., Srikram, J., Kongsune, P., 2017. Adsorption of methyl orange on coffee grounds activated carbon. Energy Proc. 138, 949–954. https://doi.org/10.1016/j.egypro.2017.10.064.
Ren, X., Xu, X., Xiao, Y., Chen, W., Song, K., 2019. Effective removal by coagulation of contaminants in concentrated leachate from municipal solid waste incineration power plants. Sci. Total Environ. 685, 392–400. https://doi.org/10.1016/j.scitotenv.2019.05.392.
Samanta, P., Desai, A.V., Let, S., Ghosh, S.K., 2019. Advanced porous materials for sensing, capture and detoxification of organic pollutants toward water remediation. ACS Sustain. Chem. Eng. 7, 7456–7478. https://doi.org/10.1021/acssuschemeng.9b00155.
Sepehr, M.N., Amrane, A., Karimaian, K.A., Zarrabi, M., Ghaffari, H.R., 2014. Potential of waste pumice and surface modified pumice for hexavalent chromium removal: characterization, equilibrium, thermodynamic and kinetic study. J. Taiwan Inst. Chem. Eng. 45, 635–647. https://doi.org/10.1016/j.jtice.2013.07.005.
Shah, S.S.A., Najam, T., Hafeez, A., Waseem, A., 2017. Nano-metal organic frame work an excellent tool for biomedical imaging. Curr. Med. Imag. Rev. 13 https://doi.org/10.2174/1573405613666170919151454.
Shayesteh, H., Norouzbeigi, R., Rahbar-Kelishami, A., 2021a. Hydrothermal facile fabrication of superhydrophobic magnetic nanospiky nickel wires: optimization via statistical design. Surface. Interfac. 26, 101315 https://doi.org/10.1016/j.surfin.2021.101315.
Shayesteh, H., Rahbar-Kelishami, A., Norouzbeigi, R., 2022. Superhydrophobic/superoleophilic micro/nanostructure nickel particles for oil/water mixture and emulsion separation. Ceram. Int. 48, 10999–11008. https://doi.org/10.1016/j.ceramint.2021.12.320.
Shayesteh, H., Rahbar-Kelishami, A., Norouzbeigi, R., 2016. Evaluation of natural and cationic surfactant modified pumice for Congo red removal in batch mode: kinetic, equilibrium, and thermodynamic studies. J. Mol. Liq. 221, 1–11. https://doi.org/10.1016/j.molliq.2016.05.053.
Shayesteh, H., Raji, F., Kelishami, A.R., 2021b. Influence of the alkyl chain length of surfactant on adsorption process: a case study. Surface. Interfac. 22, 100806 https://doi.org/10.1016/j.surfin.2020.100806.
Sing, K.S.W., Williams, R.T., 2004. Physisorption hysteresis loops and the characterization of nanoporous materials. Adsorpt. Sci. Technol. 22, 773–782. https://doi.org/10.1260/0263617053499032.
Solís, M., Solís, A., Pérez, H.I., Manjarrez, N., Flores, M., 2012. Microbial decolouration of azo dyes: a review. Process Biochem. 47, 1723–1748. https://doi.org/10.1016/j.procbio.2012.08.014.
Srivind, J., Nagarethinam, V.S., Suganya, M., Balamurugan, S., Usharani, K., Balu, A.R., 2019. NiO coupled SnS2 nanoparticles with improved magnetic and photocatalytic performance against the degradation of organic dyes without NN double bond. Vacuum 163, 373–383. https://doi.org/10.1016/j.vacuum.2019.02.048.
Su, Y., Jiao, Y., Dou, C., Han, R., 2014. Biosorption of methyl orange from aqueous solutions using cationic surfactant-modified wheat straw in batch mode. Desalination Water Treat. 52, 6145–6155. https://doi.org/10.1080/19443994.2013.811121.
Sudhasree, S., Shakila Banu, A., Brindha, P., Kurian, G.A., 2014. Synthesis of nickel nanoparticles by chemical and green route and their comparison in respect to biological effect and toxicity. Toxicol. Environ. Chem. 96, 743–754. https://doi.org/10.1080/02772248.2014.923148.
Sun, B., Yuan, Y., Li, H., Li, X., Zhang, C., Guo, F., Liu, X., Wang, K., Zhao, X.S., 2019. Waste-cellulose-derived porous carbon adsorbents for methyl orange removal. Chem. Eng. J. 371, 55–63. https://doi.org/10.1016/j.cej.2019.04.031.
Tahazadeh, S., Karimi, H., Mohammadi, T., Emrooz, H.B.M., Tofighy, M.A., 2021. Fabrication of biodegradable cellulose acetate/MOF-derived porous carbon nanocomposite adsorbent for methylene blue removal from aqueous solutions. J. Solid State Chem. 299 https://doi.org/10.1016/j.jssc.2021.122180.
Tran, T.T. Van, Kumar, S.R., Lue, S.J., 2019. Separation mechanisms of binary dye mixtures using a PVDF ultrafiltration membrane: donnan effect and intermolecular interaction. J. Membr. Sci. 575, 38–49. https://doi.org/10.1016/j.memsci.2018.12.070.
Tsai, W.-T., Yang, J.-M., Hsu, H.-C., Lin, C.-M., Lin, K.-Y., Chiu, C.-H., 2008. Development and characterization of mesoporosity in eggshell ground by planetary ball milling. Microporous Mesoporous Mater. 111, 379–386. https://doi.org/10.1016/j.micromeso.2007.08.010.
Tsiakaras, P., 2022. Oxygen Evolution Reactions, pp. 1–9.
Wang, H., Kou, X., Zhang, J., Li, J., 2008. Large scale synthesis and characterization of Ni nanoparticles by solution reduction method. Bull. Mater. Sci. 31, 97–100. https://doi.org/10.1007/s12034-008-0017-1.
Wanyonyi, W.C., Onyari, J.M., Shiundu, P.M., 2014. Adsorption of Congo red dye from aqueous solutions using roots of eichhornia crassipes: kinetic and equilibrium studies. Energy Proc. 50, 862–869. https://doi.org/10.1016/j.egypro.2014.06.105.
Xi, Y., Sun, Z., Hreid, T., Ayoko, G.A., Frost, R.L., 2014. Bisphenol A degradation enhanced by air bubbles via advanced oxidation using in situ generated ferrous ions from nano zero-valent iron/palygorskite composite materials. Chem. Eng. J. 247, 66–74. https://doi.org/10.1016/j.cej.2014.02.077.
Xu, J., Liu, S., Liu, Y., 2016. Co3O4/ZnO nanoheterostructure derived from core-shell ZIF-8@ZIF-67 for supercapacitors. RSC Adv. 6, 52137–52142. https://doi.org/10.1039/c6ra07773k.
Yan, X., Li, X., Yan, Z., Komarneni, S., 2014. Porous carbons prepared by direct carbonization of MOFs for supercapacitors. Appl. Surf. Sci. 308, 306–310. https://doi.org/10.1016/j.apsusc.2014.04.160.
Yang, M., Bai, Q., 2019. Flower-like hierarchical Ni-Zn MOF microspheres: efficient adsorbents for dye removal. Colloids Surfaces A Physicochem. Eng. Asp. 582, 123795 https://doi.org/10.1016/j.colsurfa.2019.123795.
Yang, W., Liu, X., Li, D., Fan, L., Li, Y., 2015. Aggregation-induced preparation of ultrastable zinc sulfide colloidal nanospheres and their photocatalytic degradation of multiple organic dyes. Phys. Chem. Chem. Phys. 17, 14532–14541. https://doi.org/10.1039/C5CP01831E.
Zdravkov, B.D., Čermák, J.J., Šefara, M., Janků, J., 2007. Pore classification in the characterization of porous materials: a perspective. Cent. Eur. J. Chem. 5, 385–395. https://doi.org/10.2478/s11532-007-0017-9.
Zhai, L., Bai, Z., Zhu, Y., Wang, B., Luo, W., 2018. Fabrication of chitosan microspheres for efficient adsorption of methyl orange. Chin. J. Chem. Eng. 26, 657–666. https://doi.org/10.1016/j.cjche.2017.08.015.
Zhang, K., Huo, Q., Zhou, Y.-Y., Wang, H.-H., Li, G.-P., Wang, Y.-W., Wang, Y.-Y., 2019. Textiles/metal–organic frameworks composites as flexible air filters for efficient particulate matter removal. ACS Appl. Mater. Interfaces 11, 17368–17374. https://doi.org/10.1021/acsami.9b01734.
Zhang, K., Yang, Z., Mao, X., Chen, X.-L., Li, H.-H., Wang, Y.-Y., 2020. Multifunctional textiles/Metal−Organic frameworks composites for efficient ultraviolet radiation blocking and noise reduction. ACS Appl. Mater. Interfaces 12, 55316–55323. https://doi.org/10.1021/acsami.0c18147.
Zhang, Y., Li, Y., Zhang, X., Tan, T., 2015. Biodiesel production by direct transesterification of microalgal biomass with co-solvent. Bioresour. Technol. 196, 712–715. https://doi.org/10.1016/j.biortech.2015.07.052.